Fe-doping modulated critical behavior and magnetocaloric effect of magnetic Weyl $Co_3Sn_2S_2$

Jiyu Hu,[1] Zheng Chen,[2,*] Meiling Wang,[1] Min Wang,[1] Shouguo Wang,[1] Ganhong Zheng,[1] Xin Liang,[3] Wenjian Lu,[3] and Yongqing Ma[1,†]

[1]*School of Materials Science and Engineering, Anhui University, Hefei 230039, China*

[2]*Anhui Province Key Laboratory of Condensed Matter Physics at Extreme Conditions, High Magnetic Field Laboratory, Chinese Academy of Sciences, Hefei 230031, China*

[3]*Institute of Solid State Physics, Chinese Academy of Sciences, Hefei 230031, China*

(Received 22 September 2022; revised 29 November 2022; accepted 2 February 2023; published 7 March 2023)

$Co_{2.5}Fe_{0.5}Sn_2S_2$ single crystal was grown by a flux method, and its magnetocaloric effect and critical behavior were systematically investigated. Significant changes in magnetic properties and critical behavior were observed in Fe-doped $Co_3Sn_2S_2$, compared with undoped $Co_3Sn_2S_2$. Specifically, the magnetization of $Co_{2.5}Fe_{0.5}Sn_2S_2$ measured at a low magnetic field ($H < 500$ Oe, $H \| c$ axis) does not show the thermal hysteresis phenomenon, whereas it was observed in $Co_3Sn_2S_2$ near T_c, which is characteristic of a typical second-order phase transition. Previous reports usually attribute the suppression of ferromagnetism by the substitution of Fe for Co to the decrease in the number of $3d$ electrons. Herein, according to the first-principles calculation, the magnetic moments of dopant Fe align antiparallelly to those of Co atoms, which is also the possible reason for the decrease in magnetization. The critical behavior analysis shows that the critical exponents of the Fe-doped sample around magnetic transition are very close to theoretical values of the mean-field model. Furthermore, the exchange interaction distance $J(r) \approx r^{-4.65}$ and the Rhodes-Wolfarth ratio (RWR) (RWR > 1) prove the long-range itinerant ferromagnetism. The hybridization between the $3d$ orbitals of Fe/Co and the orbitals of Sn-$5p$/S-$3p$ may be an important factor for long-range itinerant ferromagnetism. The zero-field cooling magnetization ($H = 100$ Oe, $H \| ab$ plane) undergoes the spin reorientation around 76 K, maybe because the magnetic moments of Fe, aligning antiparallelly to moments of Co atoms, reorient from out of plane to in plane. The critical behavior analysis shows that the first-order phase transition may occur below T_c in the case of the $H \| ab$ plane.

DOI: 10.1103/PhysRevB.107.094104

I. INTRODUCTION

As a topological Weyl semimetal, the shandite-structured $Co_3Sn_2S_2$ crystal with a kagome lattice exhibits many novel physical properties, such as the giant anomalous Hall effect [1–3], the zero-field Nernst effect [4], the giant magneto-optical response [5], and the thermoelectric effect [6,7]. With regard to magnetic properties, the kagome crystal has attracted great attention due to the frustrated magnetism, which possibly produces the quantum spin liquid [8] and magnetic skyrmion phases [9–11].

Inelastic neutron scattering indicated there exists quasi-three-dimensional ferromagnetic interactions in $Co_3Sn_2S_2$ with the coupling strength in intralayer being twice larger than that of interlayer [12]. Using the muon spin rotation method, Guguchia *et al.* revealed that the out-of-plane ferromagnetic ground state coexists with the in-plane antiferromagnetic state above 90 K in $Co_3Sn_2S_2$ [13], whereas, Lachman *et al.* observed the spin glass behavior and exchange bias phenomenon in $Co_3Sn_2S_2$ below T_c [14]. Moreover, the effects of doping at Co, Sn, and S sites on the magnetic properties of $Co_3Sn_2S_2$ have been widely investigated for the purpose of deep insight into the magnetism of $Co_3Sn_2S_2$ and in order to find novel physical phenomena.

Ni and Fe are usually selected to replace Co [15,16]. For the $Co_{3-x}Ni_xSn_2S_2$ single crystals [15], the Ni doping reduces the saturation magnetic moment to the lowest value of 0.03 μ_B/f.u. at 2 K ($x = 0.6$) ($H \| c$), much lower than that (0.9 μ_B/f.u.) for $Co_3Sn_2S_2$ but greatly increases the coercivity ($H_c = 1.2$ T at $x = 0.2$). The reduced moment due to the Ni doping is attributed to the increase in the spacing (d_{Co-Co}) between the nearest-neighboring Co atoms and to the change in the energy band. Importantly, the significant anomalous Hall conductance appears at the moderate Ni content, experimentally confirming that the topological properties of $Co_3Sn_2S_2$ are preserved under the Ni doping. For the $(Co_{1-x}Ni_x)_3Sn_2S_2$ polycrystalline sample, the magnetic susceptibility decreases with the increase in Ni content, and the ferromagnetism was completely destroyed at $x = 0.2$ without the appearance of the antiferromagnetic phase in all Ni-doped samples; the decrease in susceptibility due to the Ni doping is attributed to the increase in the number of $3d$ electrons [17]. For $Co_3In_2S_2$, the substitution of Fe for Co induces the antiferromagnetic transition in $(Co_{1-x}Fe_x)_3In_2S_2$ at low temperature [18], and the antiferromagnetic transition temperature T_N increases from 11 to 17 K as the Fe content increases from $x = 0.025$ to $x = 0.046$. According to the analysis of neutron diffraction and fitting data, it is concluded that the magnetic moments

*Corresponding author: chenz911@mail.ustc.edu.cn
†mayq@ahu.edu.cn

arrange antiferromagnetically with the 120 °-like structure in the kagome layer and the 45 ° canting out of the plane, resulting in a net magnetic moment of about 0.14 μ_B/Co(Fe) in the *c*-axis direction. Meanwhile, a large, linear, nonsaturated magnetoresistance is also observed in the Fe-doped samples. Kassem *et al.* found that both Fe- and In-doped (hole-doped) $Co_3Sn_2S_2$ exhibited almost the same magnetic phase diagram, which means that the number of electrons plays a decisive role in the magnetic properties of $Co_3Sn_2S_2$ crystals [16].

The In element is usually chosen as the dopant at the Sn site [19]. The In doping results in the distortion of lattice and electronic structures, whereas the lattice distortion caused by Fe replacing Co is smaller [20]. The cell parameter *a* decreases, and *c* increases with increasing the In content for $Co_3Sn_{2-x}In_xS_2$ single crystals [21]. The dopant In inhibits the ferromagnetic order; the ferromagnetic order disappears at $x = 0.8$, and the sample changes from a ferromagnetic Weyl semimetal to a nonmagnetic insulator [22]. The magnetization for the sample with $x = 0.84$ exhibits a divergent behavior with the temperature approaching 0 K, attributed to the ferromagnetic quantum criticality. The samples with $x > 0.84$ exhibit the Pauli paramagnetic behavior. The suppression of the ferromagnetic order by the In doping was attributed to the decrease in the number of electrons because the out-shell electronic configuration is $5s^25p^1$ for the In element, whereas, it is $5s^25p^2$ for the Sn element. For $Co_3Sn_{2-x}In_xS_2$ ($0 \leqslant x \leqslant 2$) and $Co_{3-y}Fe_ySn_2S_2$ ($0 \leqslant y \leqslant 0.5$) single crystals, the Curie temperature, effective magnetic moment, and spontaneous magnetization change with the increase in the In and Fe contents almost in the same trend, indicating that the number of electrons play an important role in magnetism [23].

The S element occupies the interlayer of the kagome lattice in $Co_3Sn_2S_2$. The substitution Se for S reduces the magnetic transition temperature T_c and the magnetization but does not cause the magnetic phase transition in the whole doping range. The effect of Se doping on magnetic properties is not as significant as that for In and Ni dopings [24,25].

According to the above results, it can be found that both electron and hole doping at Co or Sn sites suppresses the ferromagnetism of $Co_3Sn_2S_2$, and it is considered that the number of electrons plays an important role in magnetism in this itinerant system. Besides the number of electrons, the magnetism of $Co_3Sn_2S_2$ is also sensitive to other factors, such as the occupied positions of the dopant (within or between kagome layers) and the distortion of the crystal/electronic structure caused by dopant, which affect the interaction of magnetic ions intra- or interkagome layers and, hence, the magnetism. The usual magnetization measurements can only observe the changes in T_c and magnetization magnitude caused by the dopant. Herein, the magnetocaloric effect and critical behavior near the magnetic transition for the Fe-doped $Co_3Sn_2S_2$ were investigated in order to explore the essence of magnetic ground state [26–30].

The magnetocaloric effect and critical behavior have been widely used to investigate molecular nanomagnets [31], alloys [32,33], perovskite manganese oxides, spinel ferrites, and quantum spin liquid substances [34,35]. Recently, we investigated the critical behavior and magnetocaloric effect of undoped $Co_3Sn_2S_2$ and provided the possible magnetic phase diagram [36]. The results of critical behavior show that the magnetic order state along the *c* axis conforms to the three-dimensional Ising model. So far, the critical behavior and magnetocaloric effect of Fe-doped $Co_3Sn_2S_2$ (hole doping) have not been investigated. In this paper, we investigated the critical behavior and magnetocaloric effects of $Co_{2.5}Fe_{0.5}Sn_2S_2$. Besides the decrease in magnetization and T_c caused by the Fe doping, it is also observed that the critical behavior of $Co_{2.5}Fe_{0.5}Sn_2S_2$ is obviously different from that of $Co_3Sn_2S_2$.

II. EXPERIMENTAL DETAILS

A. Sample preparation

The single crystal of $Co_{2.5}Fe_{0.5}Sn_2S_2$ was synthesized by a flux method. The high-purity powders of Co (99.99% purity, China New Metal Materials Technology), Fe (99.99% purity, China New Metal Materials Technology), Sn (99.99% purity, China New Metal Materials Technology), and S (99.99% purity, Aladdin) were uniformly mixed with the Co:Fe:Sn:S = 6.7:1.4:86:6 ratio and sealed in a quartz tube, heated to 1000 °C and held for 10 h. The flux Sn was removed by centrifugation at 1600 r/min after another 7 days of slow cooling to 700 °C, and finally the single crystal was obtained.

B. Sample Characterization

The crystal structure of $Co_{2.5}Fe_{0.5}Sn_2S_2$ single crystal was characterized by x-ray diffraction [(XRD), Rigaku D/max-2550 V/PC] at room temperature with Cu Kα ($\lambda = 1.5406$ Å) radiation. To determine the composition of the sample, the energy-dispersive x-ray spectroscopy was measured six times, and the atomic ratio of Co:Fe:Sn:S is approximately 2.5:0.5:2:2.

The Quantum Design superconducting quantum interference device magnetic property measurement system 3 is used to measure the temperature-dependent magnetization $M(T)$ and magnetic field-dependent magnetization $M(H)$. The sample is cooled from room temperature to 5 K without the applied magnetic field and then warmed up to 400 K under the applied magnetic field. The magnetization was collected during the warming process, i.e., the zero-field-cooling (ZFC) magnetization. The magnetization, recorded during cooling the sample from 400 to 5 K under the magnetic field, is denoted as fcc magnetization, and the magnetization collected during warming from 5 to 400 K is referred to as field-cooled warming (FCW) magnetization. The initial magnetization $M(H)$ is measured as the magnetic field H increases from 0 to 50 kOe at different temperatures. The magnetic hysteresis loop is measured in the range of −50–+50 kOe at temperatures of 5 and 300 K, respectively. The resistivity was tested by physical property measurement system-9T.

III. RESULTS AND DISCUSSION

A. The crystal structure of $Co_{2.5}Fe_{0.5}Sn_2S_2$

Figure 1(a) shows the XRD pattern of the $Co_{2.5}Fe_{0.5}Sn_2S_2$ single crystal. The three diffraction peaks correspond to the diffraction of (003), (006), and (009) crystal planes, consistent with the results reported in the literature [36–38], indicating that $Co_{2.5}Fe_{0.5}Sn_2S_2$ crystallizes the rhombohedral system

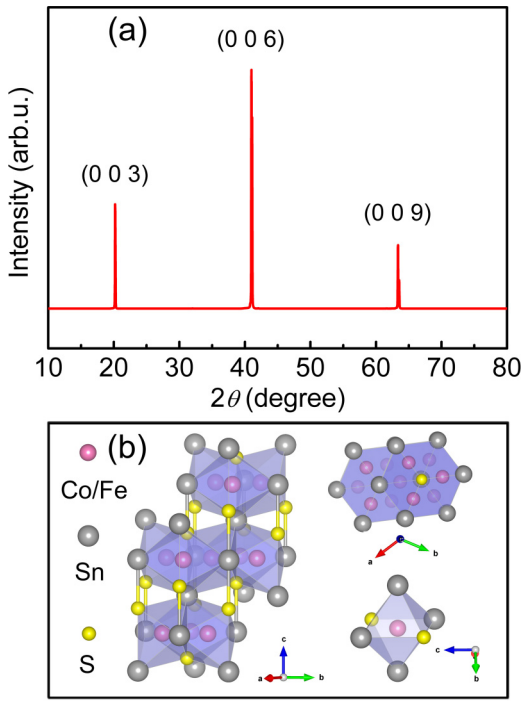

FIG. 1. (a) XRD patterns of the $Co_{2.5}Fe_{0.5}Sn_2S_2$ single crystal. (b) The crystal cell of $Co_{2.5}Fe_{0.5}Sn_2S_2$.

with the R-3m (No.166) space group [1,15,39]. Figure 1(b) shows the crystal cell of the $Co_{2.5}Fe_{0.5}Sn_2S_2$ single crystal. The kagome layer is a regular hexagonal kagome unit composed of Co(Fe) atoms and Sn atoms in which the Co(Fe) atoms are located at the apex of the regular hexagon. The special crystal structure makes the magnetic moments of Co(Fe) in the kagome layer form a frustrated state. The Sn atom is distributed between the kagome layer and the kagome layer, whereas, the S atom is located between the kagome layers.

B. The magnetic properties of $Co_{2.5}Fe_{0.5}Sn_2S_2$

Figures 2(a)–2(e) show the relationship between magnetization (M) and temperature (T) with the $H \| c$ axis. Figure 2(a) shows the $M(T)$ curve measured under $H = 100$ Oe, exhibiting a steep transition with decreasing temperature. Accordingly, the derivative curve of ZFC magnetization shows a minimum at a certain temperature, which is defined as the paramagnetic-ferromagnetic transition temperature T_c. The T_c value of $Co_{2.5}Fe_{0.5}Sn_2S_2$ is 104 K as $H = 100$ Oe, close to that reported in the literature [16]; this T_c value is lower than that ($T_c = 174$ K) of undoped $Co_3Sn_2S_2$, indicating that the Fe doping significantly suppresses ferromagnetism [16,36]. The bifurcation between the ZFC and the fcc curves below T_c and the local maximum around 87 K in the ZFC curve were also observed previously [14,39]. For $Co_3Sn_2S_2$, there exhibits the thermal hysteresis behavior between the fcc and the FCW curves below T_c, which generally does not occur for the normal second-order phase transition [12,36,39]. Such hysteresis behavior results from the phase-separation state due to the coexistence of ferromagnetic and antiferromagnetic (or spin glass) phases [13,14]. However, the fcc and FCW curves of $Co_{2.5}Fe_{0.5}Sn_2S_2$ do not show the hysteresis, characteristic of the second-order phase transition [29].

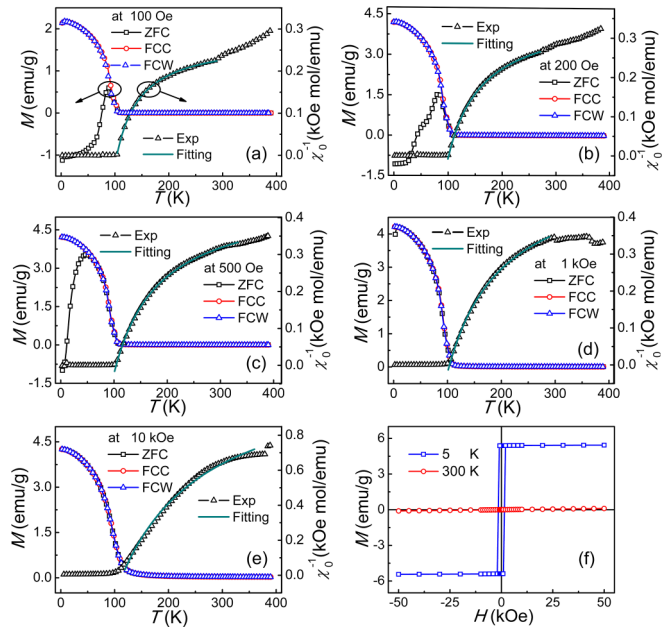

FIG. 2. The temperature-dependent magnetization $M(T)$ with the ZFC (black empty squares), fcc (red empty circles), and FCW (blue empty triangles) processes measured at different applied magnetic fields (H) [(a)–(e)] together with the inverse susceptibility (empty triangles) and its fitting curves (solid lines). The H-dependent magnetization $M(H)$ curves, i.e., magnetic hysteresis loops recorded at 5 and 300 K (f) for $H \| c$ axis.

The ZFC and fcc curves almost overlap as $H \geqslant 1$ kOe [Figs. 2(d) and 2(e)], which is due to the fully polarized state in the temperature region below T_c [13]. In Fig. 2(f), $M(H)$ measured at 5 K rapidly saturates with increasing the magnetic field because the c axis is the magnetic easy axis. The saturation magnetization M_s is 5.43 emu/g, i.e., the saturation moment μ_s is 0.16 μ_B/Co(Fe), much smaller than that of $Co_3Sn_2S_2$ (0.3 μ_B/Co) [1], further indicating that Fe (hole) doping suppresses ferromagnetism [16]. The Ni (electron) doping can also suppress ferromagnetism, i.e., both hole and electron dopings suppress ferromagnetism [15]. So, the conclusion, attributing the suppressed ferromagnetism to the 3d electron number of the doped element, is open to deliberation, deserving further investigation. According to $M(H)$ at 5 K in Fig. 2(f), the ratio of remanent magnetization M_r to saturation magnetization M_s, i.e. M_r/M_s is 0.99, close to the theoretical remanent magnetization ratio of a uniaxial anisotropic magnet ($M_r/M_s = 1$), indicative of the uniaxial anisotropy for $Co_{2.5}Fe_{0.5}Sn_2S_2$. $M(H)$ at 300 K shows the paramagnetic characteristic due to the random orientation of moments caused by the thermal fluctuation.

Based on the ZFC curve in the paramagnetic region in Figs. 2(a)–2(e), we can obtain the temperature-dependent inverse susceptibility $\chi_0^{-1}(T)$. The modified Curie-Weiss law is expressed as

$$\chi_0^{-1}(T) = \left(\frac{C}{T - T_\theta} + \chi_0\right)^{-1} \quad (1)$$

The Curie-Weiss constant C is obtained after the fitting of $\chi_0^{-1}(T)$ above T_c [29]. The effective magnetic

TABLE I. Parameters from the fitting according to equation $\chi_0^{-1}(T) = (\frac{C}{T-T_\theta} + \chi_0)^{-1}$ and calculated $\mu_{\rm eff}$ and μ_c for $H \| c$.

$H \parallel c$ (Oe)	T_c (K)	C (emu K/Oe mol)	T_θ (K)	$\mu_{\rm eff}$ [μ_B/Co(Fe)]	μ_c [μ_B/Co(Fe)]
100	104	0.161	104	0.656	0.196
200	92	0.183	103	0.699	0.220
500	91	0.191	105	0.714	0.229
1000	91	0.192	105	0.716	0.230
10000	97	0.137	114	0.605	0.169

moment of $Co_{2.5}Fe_{0.5}Sn_2S_2$ can be calculated from $\mu_{\rm eff} = 2.83(C/\eta)^{0.5}\mu_B$, where η is the number of magnetic atoms in the unit cell. The fitted parameters C and θ and calculated $\mu_{\rm eff}$ under different magnetic fields are listed in Table I. The value of μ_c, which is related to the number of moving carriers [29], can be calculated from $\mu_{\rm eff}^2 = (\mu_c + 2)\mu_c$. Furthermore, the Rhodes-Wolfarth ratio (RWR) can be obtained according to RWR $= \mu_c/\mu_s$ [40,41]. RWR $= 1$ indicates that magnetization comes from the contribution of local magnetic moment, whereas RWR > 1 is the evidence of itinerant ferromagnetism. It can be seen from Table I that $Co_{2.5}Fe_{0.5}Sn_2S_2$ is characteristic of the itinerant ferromagnetism along the c axis.

Figures 3(a)–3(c) show the $M(T)$ curves measured under the $H \| ab$ plane. The ZFC curve as $H = 100$ Oe first shows a maximum at 104 K. Then, it shows a minimum at 73 K and a flat in the low-temperature region; this phenomenon may originate from the reorientation of Fe magnetic moments, which will be further understood in the first-principles calculation section. The bifurcation between ZFC and fcc still exists as $H > 1$ kOe because the complete polarization cannot be reached as $H \| ab$ due to the spin frustration behavior in the kagome layer. As shown in Fig. 3(d), the $M(H)$ curve measured at 5 K does not saturate as $H = 50$ kOe due to the magnetic frustration behavior. The inverse susceptibility in the temperature region above T_c can still be well fitted by Eq. (1), and the fitted parameters are listed in Table II. It can be seen from Tables I and II that the effective magnetic moment $\mu_{\rm eff}$ and μ_c as $H \| ab$ is larger than those as $H \| c$ under the same applied magnetic field, even though the magnetic moments in the ab plane are frustrated. The possible reasons are as follows. On one hand, the number of magnetic atoms within unit area on the ab plane is larger than that along the c axis due to the larger cell parameter c than a and b. On the other hand, in the direction of the c axis, the moment of Fe atoms may align antiparallelly to that of Co atoms and reorientate towards the ab plane as the magnetic field is applied on the ab plane, which will be further discussed below.

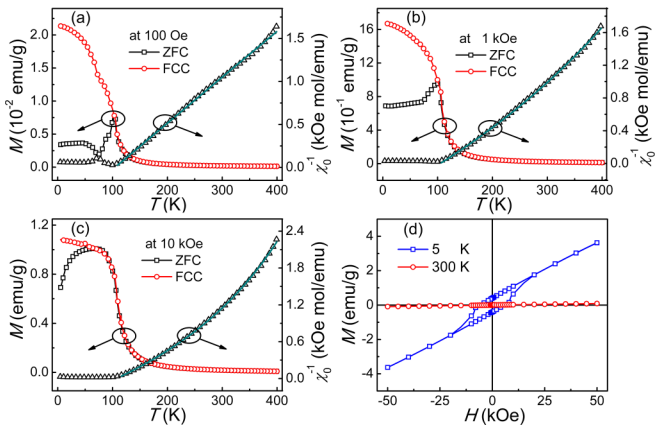

FIG. 3. The temperature-dependent magnetization $M(T)$ with the ZFC (black empty squares) and fcc (red empty circles) processes measured at different applied magnetic field (H) [(a)–(c)] together with the inverse susceptibility (empty triangle) and its fitting curves (solid lines); the H-dependent magnetization $M(H)$ curves recorded at 5 and 300 K (d) for the $H \| ab$ plane.

C. The magnetocaloric effect for $Co_{2.5}Fe_{0.5}Sn_2S_2$

Figures 4(a) and 4(b) show the isothermal magnetization curves in the temperature range of 80–130 K for magnetic-fields $H \| c$ and $H \| ab$, respectively. In the case of $H \| c$ with increasing the magnetic field, the magnetization rapidly tends to saturate below T_c, but it increases linearly above T_c. In the case of $H \| ab$, the magnetization is not saturated when H increases to 50 kOe due to the spin frustration on the ab plane.

Essentially, the magnetocaloric effect (MCE) results from the entropy change caused by the coupling between the magnetic spin system and the magnetic field [30]. Using the Maxwell relation and classical thermodynamic theory, the

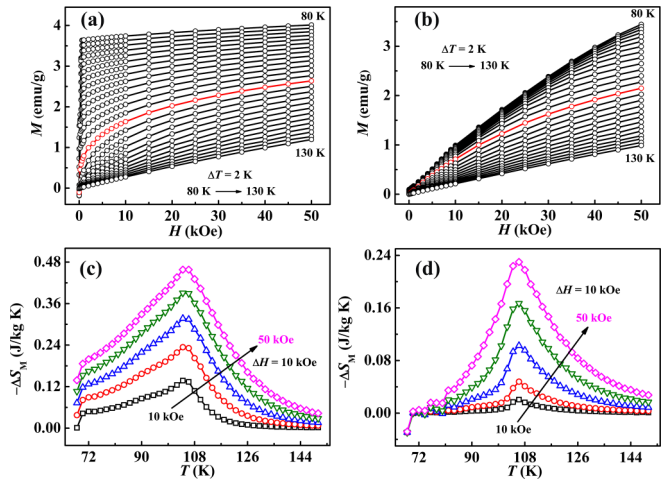

FIG. 4. Isotherm magnetization M as a function of the magnetic-field H measured in a temperature range of 80–130 K (a) and (b) and the magnetic entropy change $-\Delta S_M$ as a function of temperature T at different magnetic fields (c) and (d) with the magnetic-field $H \| c$ axis (left) and $H \| ab$ plane (right).

TABLE II. Parameters from the fitting according to equation $\chi_0^{-1}(T) = (\frac{C}{T-T_\theta} + \chi_0)^{-1}$ and calculated μ_{eff} and μ_c for $H \| ab$.

$H \| ab$ (Oe)	T_c (K)	C (emu K/Oe mol)	T_θ (K)	μ_{eff} [μ_B/Co(Fe)]	μ_c [μ_B/Co(Fe)]
100	105.7	0.185	105.2	0.703	0.222
1000	106.3	0.236	106.5	0.794	0.277
10000	106.7	0.239	107.4	0.799	0.280

magnetic entropy change $-\Delta S_M$ curve can be given from [42]

$$\Delta S_M(T,H) = S_M(T,H) - S_M(T,0) = \int_0^H \left(\frac{\partial M}{\partial T}\right)_H dH. \tag{2}$$

And, the magnetic entropy change curve with temperature in a discrete form can be approximately described as [43]

$$\Delta S_M(T,H) = \sum_i \frac{M_{i+1} - M_i}{T_{i+1} - T_i} \Delta H_i. \tag{3}$$

Here, M_i and M_{i+1} represent the magnetization values at temperatures T_i and T_{i+1} under the applied magnetic-field H_i. According to Eq. (3), the temperature-dependent $-\Delta S_M$ can be calculated from the $M(H)$ curves in Figs. 4(a) and 4(b). The calculated $-\Delta S_M$ curves are shown in Fig. 4(c) and 4(d) for the $H \| c$ axis and the $H \| ab$ plane.

In the case of the $H \| c$ axis, the maximum value of $-\Delta S_M$ appears around $T_c = 106$ K because the magnetization M changes sharpest around T_c. The maximum magnetic entropy change $-\Delta S_M^{\max}$ increases monotonically with the increase in magnetic field and reaches the maximum value of $0.46\,\text{J}\,\text{kg}^{-1}\,\text{K}^{-1}$ as $\Delta H = 50$ kOe, common for many MCE materials with the second-order phase transition, such as Pd_xCoCrFeNi [28,44].

In the case of the $H \| ab$ plane, $-\Delta S_M^{\max} = 0.26\,\text{J}\,\text{kg}^{-1}\,\text{K}^{-1}$ appears at $T_c = 106$ K as $\Delta H = 50$ kOe, less than the value with $H \| c$ due to the anisotropy of the magnetic ordering. Noticeably, $-\Delta S_M$ exhibits a weak local maximum around 77 K and a negative value below 77 K, which is related to spin reorientation ($H \| ab$). The sign of magnetic entropy change reflects the change in the magnetically ordered state, for instance, the ferromagnetic (FM) and antiferromagnetic (AFM) states correspond to $\Delta S_M < 0$ and $\Delta S_M > 0$, respectively. [39].

The relative cooling power (RCP) [45] can be determined by the equation,

$$\text{RCP} = -\Delta S_M^{\max} \delta T_{\text{FWHM}}. \tag{4}$$

Here, δT_{FWHM} represents the full peak width at half of the maximum value of the magnetic entropy change curve. The results of RCP at the $H \| c$ axis and the $H \| ab$ plane are shown in Fig. 5(a). The maximum values of RCP are 17.26 and 5.06 J/kg as the $H \| c$ axis and the $H \| ab$ plane. Figure 5(b) shows the value of the RMCE $-\Delta S_R$ [26],

$$\Delta S_R(T,H) = -\Delta S_M(T, H \parallel c) - [-\Delta S_M(T, H \parallel ab)]. \tag{5}$$

The maximum value of $-\Delta S_R$ increases, and the width of the peak broadens with increasing the magnetic field. This result shows that the magnetic entropy change can be obtained by rotating the sample from the c axis to the ab plane. The conventional magnetic entropy change is obtained by changing the magnetic field, which is difficult to apply in practice. Here, the magnetic entropy change is obtained by rotating the sample, which has certain advantages in practical applications [26].

Another important parameter of the MCE is the adiabatic temperature change ΔT_{ad} [46]. The ΔT_{ad} can be estimated by Eq. (6) [47,48],

$$\Delta T_{ad} \cong -\frac{T}{C_p} \Delta S_M(T,H). \tag{6}$$

Figure 5(c) shows the relationship between ΔT_{ad} and temperature T. The maximum values of ΔT_{ad} are 0.48 K ($H \| c$) and 0.27 K ($H \parallel ab$) at 50 kOe. These values are much smaller than the maximum ΔT_{ad} (5.33 K) at 50 kOe for a $La_{0.7}Ca_{0.3}MnO_3$ single crystal with first-order phase transition, which is common for the second-order phase-transition material [49].

The value of n can be obtained by calculating the magnetic entropy change at T_c for the $H \| c$ axis and the $H \| ab$ plane according to Eq. (7),

$$n(T,H) = dln|\Delta S_M|/dlnH \tag{7}$$

Generally, the value of n should approach 1 below T_c and 2 above T_c, respectively. n depends on the critical exponent of the material at the transition temperature, and $n > 2$

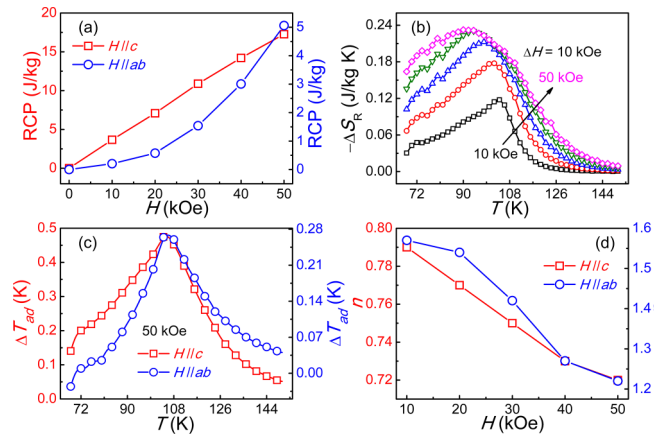

FIG. 5. (a) The magnetic-field-dependent RCP with the $H \| c$ axis and the $H \| ab$ plane. (b) Temperature dependence of the rotating magnetocaloric effect (RMCE): magnetic entropy change $-\Delta S_R$ in various magnetic fields. (c) Temperature dependence of ΔT_{ad} as $\Delta H = 50$ kOe with the $H \| c$ axis and the $H \| ab$ plane. (d) The temperature dependence of n curves with the $H \| c$ axis and the $H \| ab$ plane.

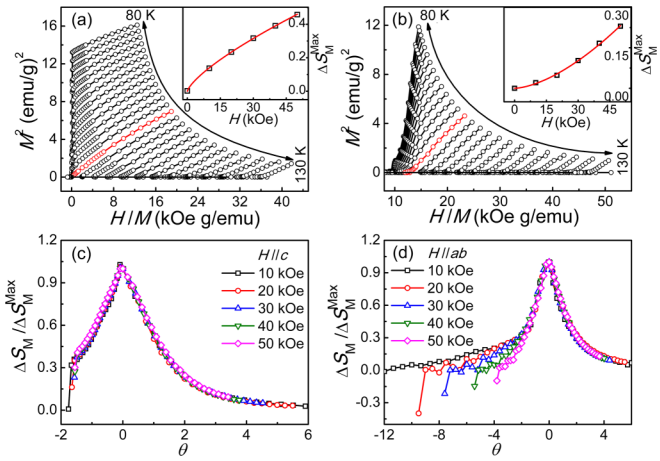

FIG. 6. (a) and (b)Arrott plots deduced from the isotherm magnetization $M(H)$ curves in the 80–130 K temperature range for the $H \| c$ axis and the $H \| ab$ plane with the magnetic-field H-dependent $-\Delta S_M^{\max}$ (empty squares) and the fitted data (solid line) according to $-\Delta S_M^{\max} = aH^n$ (the inset). (c) and (d) The reduced temperature θ dependence of the entropy $\Delta S_M / \Delta S_M^{\max}$.

is the evidence of the first-order phase transition [50]. For $Co_{2.5}Fe_{0.5}Sn_2S_2$, the n values are 0.79, 0.77, 0.75, 0.73, and 0.72 as the $H \| c$ axis, and 1.57, 1.54, 1.42, 1.27, and 1.22 as the $H \| ab$ plane as $H = 10$, 20, 30, 40, and 50 kOe, respectively. Figure 5(d) shows that the n value decreases monotonically with the increase in the magnetic field. However, the n value is larger as $H \| ab$, implying that the magnetic moment arrangement on the ab plane is more significantly affected by the magnetic field.

According to the isotherm magnetization $M(H)$ curves in Figs. 4(a) and 4(b), the Arrott diagrams ($M^2 \sim H/M$) as $H \| c$ and $H \| ab$ can be obtained as shown in Figs. 6(a) and 6(b). The $M^2 \sim H/M$ curve in the high-field region has a positive slope, corresponding to the second-order phase-transition behavior [29]. The Arrott diagram is based on the state with the mean-field criticality. If the magnetic transition conforms to the mean-field model, the corresponding $M^2 \sim H/M$ curves should be parallel straight lines at high fields. It can be seen from Fig. 6(a) that the Arrott curves are parallel above and below T_c, conforming to the mean-field model.

The relationship between the maximum magnetic entropy change $-\Delta S_M^{\max}$ near T_c and the magnetic field H can be expressed as

$$-\Delta S_M^{\max} = aH^n. \tag{8}$$

The values of $-\Delta S_M^{\max}$ at $H \| c$ and $H \| ab$ can be obtained from Figs. 4(c) and 4(d) as shown in the insets of Figs. 6(a) and 6(b), respectively. The values of n for $H \| c$ and $H \| ab$ are 0.73 and 1.60 based on the fit of Eq. (8), consistent with the results obtained in Fig. 5(d). The value of n obtained as $H \| c$ is close to the value of 0.66 for the usual second-order phase-transition material [32], and the value of n is also close to 2/3, expected for the mean-field model [51]. These results show that the magnetic transition along the c axis is a second-order phase transition, and the critical behavior near the phase transition is consistent with the mean-field model. The n value of 1.60 as $H \| ab$ indicates that the magnetic transition may be accompanied by the first-order phase transition, consistent with the result of Fig. 6(d).

The magnetic entropy change in Figs. 4(c) and 4(d) is normalized according to $\Delta S_M / \Delta S_M^{\max}$. The curve of $-\Delta S_M$ versus temperature at the half height corresponds to two temperatures: One is below T_c (denoted as T_{r1}), and the other is above T_c (denoted as T_{r2}). The reduced temperature θ is defined according to Eqs. (9) and (10),

$$\theta = -\frac{T - T_c}{T_{r1} - T_c} \quad \text{for} \quad T \leqslant T_c, \tag{9}$$

$$\theta = \frac{T - T_c}{T_{r2} - T_c} \quad \text{for} \quad T > T_c. \tag{10}$$

The dependence of $\Delta S_M / \Delta S_M^{\max}$ on θ is shown in Figs. 6(c) and 6(d). The magnetic entropy change curves at different magnetic fields almost overlap as the $H \| c$ axis, further indicating that the magnetic transition at T_c is the second-order phase transition [26]. The $\Delta S_M / \Delta S_M^{\max}$ curves do not overlap in the temperature region below 100 K as $H \| ab$, not consistent with the characteristics of the second-order phase transition, implying the possible existence of a first-order phase transition [52].

D. The critical behavior analysis of $Co_{2.5}Fe_{0.5}Sn_2S_2$

The spontaneous magnetization M_s and initial magnetic susceptibility χ_0 are obtained by linear fitting of the high-field part from the Arrott curve ($H \| c$) in Fig. 6 [29]. They were fitted according to the modified Arrott (MA) equations,

$$M_s(T) = M_0(-\varepsilon)^{\beta}, \quad \varepsilon < 0, \quad T < T_c, \tag{11}$$

$$\chi_0^{-1}(T) = (h_0/M_0)\varepsilon^{\gamma}, \quad \varepsilon > 0, \quad T > T_c, \tag{12}$$

$$M = DH^{1/\delta}, \quad \varepsilon = 0, \quad T = T_c. \tag{13}$$

Here, $\varepsilon = (T - T_c)/T_c$, and the fitting results and obtained parameters are shown in Figs. 7(a) and 7(b). Noticeably, the asymptotic critical regime (ACR) is $|\varepsilon| = |(T - T_c)/T_c| = 10^{-2}$ for homogeneous magnets and slightly larger for disordered and amorphous systems [53]. The T_c for $Co_{2.5}Fe_{0.5}Sn_2S_2$ is close to 107 K. Therefore, the ACR regime is limited to 107 ± 5.35 K if we consider an acceptable $|(T - T_c)/T_c| = 5 \times 10^{-2}$. We reduce the temperature window in the region of 100–114 K. Then, M_s and χ_0 were fitted according to Eqs. (11) and (12) (not shown here). The obtained critical exponents are $\beta = 0.506(1)$ and $\gamma = 1.015(0)$, almost the same as those obtained in the temperature window of 80 K $< T <$ 130 K and closer to those predicted by the mean-field model ($\beta = 0.5$ and $\gamma = 1.0$), indicating that these critical exponents are intrinsic values.

Another method to obtain critical parameters β and γ is the Kouvel–Fisher (KF) plot [54],

$$M_s(T)[dM_s(T)/dT]^{-1} = (T - T_c)\beta^{-1} \quad \text{for} \quad T < T_c, \tag{14}$$

$$\chi_0^{-1}(T)[d\chi_0^{-1}(T)/dT]^{-1} = (T - T_c)\gamma^{-1} \quad \text{for} \quad T > T_c. \tag{15}$$

The M_s and χ_0 are fitted, and the fitting results and parameters are shown in Fig. 7(c). The values of the critical parameters obtained by different methods, and the theoretical

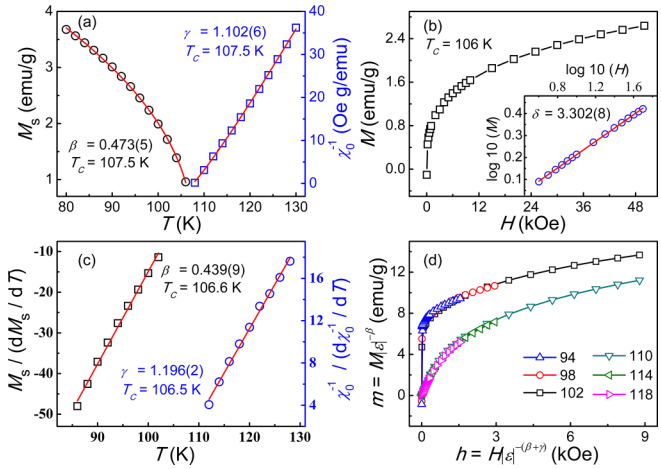

FIG. 7. (a)The temperature-dependent spontaneous magnetization M_s and inverse initial susceptibility χ_0^{-1} with the fitting solid curves according to the MA equations. (b) The critical isotherm (CI) analysis at T_c with the inset presenting the plot on the log 10-log 10 scale with a fitted solid line. (c) KF plots (empty symbols) for $M_s(T)$ and $\chi_0^{-1}(T)$ and the fitted data (solid lines) according to the KF equations. (d) Scaling plots around T_c using the values of β and γ determined by the MA.

values of the critical parameters for several major theoretical models are given in Table III. In contrast, the critical exponents of $Co_3Sn_2S_2$ are also listed in Table III, and they are closer to the 3D-Ising model, mainly due to the coexistence of the antiferromagnetic phase, the spin-glass phase, and the ferromagnetic phase [36]. Herein, the critical parameters of $Co_{2.5}Fe_{0.5}Sn_2S_2$ are closer to the mean-field model, indicating the existence of long-range magnetic interactions, and the spin fluctuation phenomenon can be ignored. The fact that there is no thermal hysteresis in the fcc and FCW curves below T_c also confirms the existence of a homogeneous ferromagnetic order.

Stanley pointed out that the magnetization in the asymptotically critical region can be expressed by the following scaling equation [55]:

$$M(H,\varepsilon) = \varepsilon^{\beta} f_{\pm}(H/\varepsilon^{\beta+\gamma}), \tag{16}$$

where $f_{\pm}$ is a regular function with f_+ for $T > T_c$ and f_- for $T < T_c$. Therefore, the relationship between the renormalized magnetization $[m \equiv \varepsilon^{-\beta} M(H,\varepsilon)]$ and the renormalized field $(h \equiv H\varepsilon^{-(\beta+\gamma)})$ is $m = f \pm (h)$. The $m(h)$ curves near the T_c based on the scalar equation are shown in Fig. 7(d), and all the magnetization curves are collapsed onto two universal curves. The critical exponents β and γ in Eq. (16) adopt those obtained by the MA method. These parameters are in good agreement with the scaling equation, confirming their reliability.

The critical exponents γ, β, and δ satisfy the Widom scaling relation according to the statistical theory [56],

$$\delta = 1 + \gamma/\beta. \tag{17}$$

The β and γ values obtained by the MA and KF methods are calculated according to Eq. (17), and the obtained δ values are 3.328(6) and 3.719(3), and the absolute errors of the δ values are 0.0258 and 0.4165, compared with $\delta = 3.302(8)$ derived from the critical isotherm analysis in Fig. 7(b). In comparison, the critical exponents obtained by MA are more consistent with the Widom scalar relation and closer to the critical parameter values ($\beta = 0.5$, $\gamma = 1.0$, and $\delta = 3$) of the mean-field model.

Finally, the essence of magnetic interaction is further analyzed according to the critical exponents obtained by the MA method. According to the Arrott-Noakes equation of state, the relationship between H/M and M follows $(H/M)^{1/\gamma} = (T - T_c)/T_c + (M/M_1)^{1/\beta}$. Here M_1 is a constant, and this equation is strictly true only as the temperature approaches T_c [57]. In general, H/M and M satisfy the following relationship:

$$(H/M)^{1/\gamma} = C_1 + C_2 M^{1/\beta}, \tag{18}$$

where C_1 and C_2 are temperature-dependent coefficients [58]. The relationship curve between $(H/M)^{1/\gamma}$ and $M^{1/\beta}$ is shown in Fig. 8, which can be obtained from Fig. 4(a) based on Eq. (18). All the curves in the high field are almost parallel

TABLE III. The critical exponents obtained by different theoretical models for $Co_{2.5}Fe_{0.5}Sn_2S_2$ with $H \| c$ and the critical exponents of several main theoretical models. LR: long range; RG-ϵ': renormalization-group epsilon (ϵ' $= 2\sigma - d$).

Composition	Technique	T_c (K)	β	γ	δ
$Co_{2.5}Fe_{0.5}Sn_2S_2$	MA	107.5	0.473	1.102	
$Co_3Sn_2S_2$		175.5	0.337	1.178	
$Co_{2.5}Fe_{0.5}Sn_2S_2$	KF	106.5	0.439	1.196	
$Co_3Sn_2S_2$		175.6	0.275	1.156	
$Co_{2.5}Fe_{0.5}Sn_2S_2$	CI	106.0			3.302
$Co_3Sn_2S_2$		176.0			4.594
Mean-field model	Theory		0.5	1.0	3.0
Tricritical mean-field model	Theory		0.25	1.0	5.0
Three-dimensional (3D)-Heisenberg model	Theory		0.365	1.386	4.8
3D-Ising model	Theory		0.325	1.24	4.82
LR exchange: $J(r) = 1/r^{d+\sigma}$					
$d = 3, n = 3, \sigma = 1.6469$	RG-ϵ'		0.7190	1.1026	2.5335
$d = 2, n = 3, \sigma = 1.0963$	RG-ϵ'		0.7217	1.1026	2.5278
$d = 2, n = 2, \sigma = 1.1086$	RG-ϵ'		0.7015	1.1026	2.5718
$d = 2, n = 1, \sigma = 1.1290$	RG-ϵ'		0.6689	1.1026	2.6484

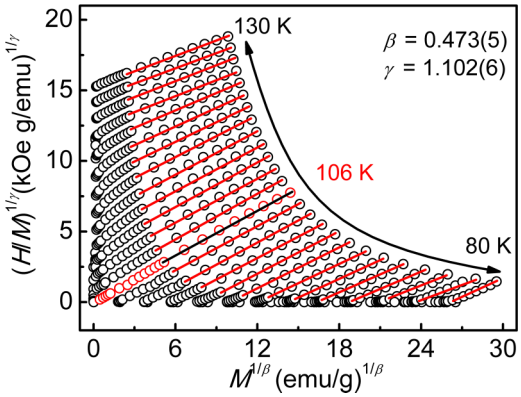

FIG. 8. The $(H/M)^{1/\gamma}$ versus $M^{1/\beta}$ using the critical exponents obtained by the MA fitting.

to each other, which indicates that the magnetization along the c axis is in good agreement with the mean-field model.

The magnetic phase transition depends on the exchange interaction $J(r)$ for a homogeneous magnet [59,60]. The renormalization-group theory gives $J(r) \sim r^{-(d+\sigma)}$, where γ, n, d, and σ satisfy the following equations:

$$\gamma = 1 + \frac{4(n+2)}{d(n+8)}\Delta\sigma + \frac{8(n+2)(n-4)}{d^2(n+8)^2} \times \left[1 + \frac{2G\left(\frac{d}{2}\right)(7n+20)}{(n-4)(n+8)}\right]\Delta\sigma^2, \quad (19)$$

$$\Delta\sigma = \left(\sigma - \frac{d}{2}\right), \quad (20)$$

$$G(d/2) = 3 - (d/2)^2/4. \quad (21)$$

Here, γ, n, d, and σ are the critical exponent, the spin dimensionality, the spatial dimension, and a constant, respectively [29,61]. A three-dimensional system with $d = 3$ gives $J(r) \approx r^{-3-\sigma}$. $\sigma \leqslant 3/2$ corresponds to the mean-field model ($\beta = 0.5$, $\gamma = 1.0$, and $\delta = 3.0$), giving $J(r) \propto r^{-4.5}$. $\sigma \geqslant 2$ corresponds to the 3D-Heisenberg ($\beta = 0.365$, $\gamma = 1.386$, and $\delta = 4.8$), giving $J(r) \propto r^{-5}$ [62]. The critical parameter $\gamma = 1.1026$ in Table III is calculated by Eqs. (19) to obtain $\sigma = 1.6469$, and, hence, $J(r) \approx r^{-4.6469}$. This is very close to the $J(r) \approx r^{-4.7}$ for the antiperovskite ferromagnetic $AlCMn_3$,

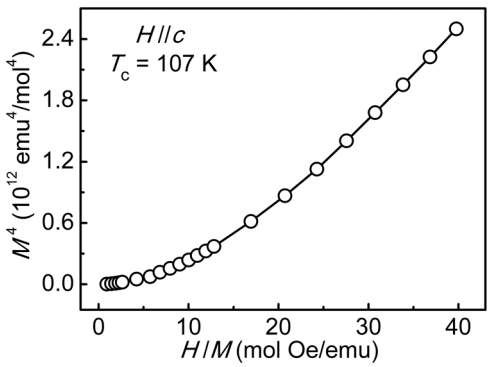

FIG. 9. The M^4 versus H/M plot for the $Co_{2.5}Fe_{0.5}Sn_2S_2$ single crystal at $T_c = 107$ K for the $H \| c$.

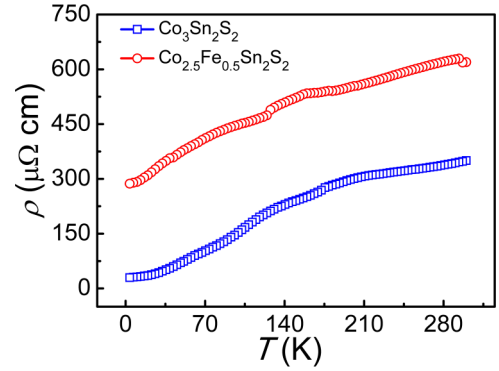

FIG. 10. The temperature-dependent resistivity of $Co_{2.5}Fe_{0.5}Sn_2S_2$ and $Co_3Sn_2S_2$.

further indicating that the sample has the long-range ferromagnetic interaction along the c axis [58]. Using Eq. (19) together with different scaling relations predicted by the scaling hypothesis, such as $\alpha = 2 - \nu d$, $\beta = (2 - \alpha - \gamma)$, and $\delta = 1 + \gamma/\beta$, the values of d, n, and σ, which yield values of critical exponents close to that found experimentally for $Co_{2.5}Fe_{0.5}Sn_2S_2$, can be calculated [63]. To do so, the value of σ is initially adjusted in Eq. (19) for several sets of $\{d{:}n\}$ to obtain a proper value of γ that matches well with the experimental value of $\gamma = 1.1026$. The obtained σ is, then, used to calculate other critical exponents from the scaling relations mentioned before. The calculated critical exponents for several sets of $d{:}n$ and obtained σ values are compiled in Table III. From Table III, we can see that for $\{d{:}n\} = 3{:}3$, 2:3, and 2:2, the calculated values of the critical exponents β and δ are significantly larger than the experimental value. Relatively, the critical exponents β and δ with $\{d{:}n\} = 2{:}1$ are closer to the experimental ones, indicating the magnetism in $Co_{2.5}Fe_{0.5}Sn_2S_2$ is quasione dimensional ($n = 1$) in nature,

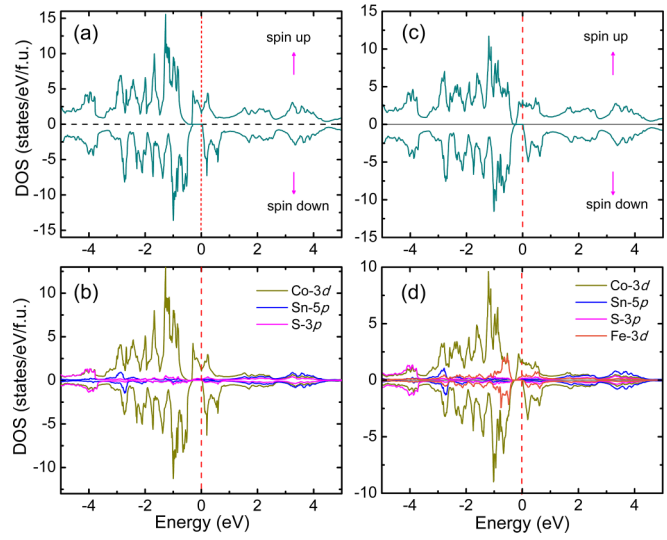

FIG. 11. The Fermi level is set to be 0 eV. The positive and negative values represent the density of states of up and down spins, respectively. (a) Total and (b) atom-orbital-projected density of states (DOS) of $Co_3Sn_2S_2$. (c) Total and (d) atom-orbital-projected DOS of $Co_{2.5}Fe_{0.5}Sn_2S_2$ under spin-up and spin-down states.

TABLE IV. Calculated $N(E_F)$, ΔE_{ex} (eV), m, I, and $N(E_F)I$ for $Co_3Sn_2S_2$ and $Co_{2.5}Fe_{0.5}Sn_2S_2$.

	$N(E_F)$ (states/eV/f.u./spin)	ΔE_{ex} (eV)	m (μ_B/atom)	I (eV)	$N(E_F)I$
$Co_3Sn_2S_2$	3.57	0.28	0.36	0.78	2.78
$Co_{2.5}Fe_{0.5}Sn_2S_3$	4.12	0.18	0.18	1.00	4.12

and the difference of β and δ between the calculated and the experimental values may result from the kagome lattice of $Co_{2.5}Fe_{0.5}Sn_2S_2$. which results in the noncollinear moments along the c axis.

For more insights into the nature of the itinerant character of $Co_{2.5}Fe_{0.5}Sn_2S_2$, the magnetic isotherm at T_c is analyzed based on the Takahashi's self-consistent renormalization theory for itinerant systems, which obeys the equation [63,64],

$$M^4 = 1.17 \times 10^{18}\left(\frac{T_c^2}{T_A^3}\right)\left(\frac{H}{M}\right), \tag{22}$$

where M and H are in units of emu/mol and Oe, respectively. T_A (in K) is the dispersion of the spin fluctuation spectrum in wave-vector space. The M^4 versus H/M plot for the $Co_{2.5}Fe_{0.5}Sn_2S_2$ single crystal at $T_c = 107$ K for the $H \| c$ as shown in Fig. 9, exhibits the concave behavior. As reported in Refs. [65–67]. The M^4 versus H/M curve exhibits the linear behavior for SmCoAsO and $LaCo_2P_2$, and the convex one for pure Co and LaCoAsO. These facts indicate that the FM state of $Co_{2.5}Fe_{0.5}Sn_2S_2$ is different from that for SmCoAsO, $LaCo_2P_2$, Co, and LaCoAsO may be due to its unique kagome lattice and frustrated magnetism.

The electrical resistivity of $Co_{2.5}Fe_{0.5}Sn_2S_2$ increases as a function of temperature, indicating metallic behavior (Fig. 10). As a comparison, the resistivity of undoped $Co_3Sn_2S_2$ was also measured. Obviously, the Fe doping increases the resistivity, maybe due to the small increase in the separation between the kagome layers and the disorder induced by the Fe doping [68].

To further investigate the origin of the long-range magnetic ordering of $Co_{2.5}Fe_{0.5}Sn_2S_2$, the first-principles calculations (Vienna *ab initio* simulation package) are performed, and the results are shown in Fig. 11. For comparison, the results of $Co_3Sn_2S_2$ are also shown in Fig. 11. The significant results obtained from the calculations are presented in Tables IV and V, respectively. The Stoner criterion of magnetic ordering can be expressed as $N(E_F)I > 1$, where $N(E_F)$ represents the DOS at the Fermi level, and I is the Stoner exchange parameter. It can be estimated according to $\Delta E_{ex} = mI$, where ΔE_{ex} and m are exchange splitting energy and magnetic moment, respectively [69]. The ΔE_{ex} between the spin-up and the spin-down energy bands of $Co_3Sn_2S_2$ and $Co_{2.5}Fe_{0.5}Sn_2S_2$ can be calculated from the results in Figs. 11(a) and 11(c). The collinear ferromagnetic configuration is considered in the calculation. It can be seen from Table IV that both $Co_3Sn_2S_2$ and $Co_{2.5}Fe_{0.5}Sn_2S_2$ satisfy the Stoner criterion $N(E_F)I > 1$, which further confirms the existence of the long-range ferromagnetism. It can be seen from Table V that the magnetic moment of Fe in the $Co_{2.5}Fe_{0.5}Sn_2S_2$ sample is negative (-0.265 μ_B/atom), which means that the magnetic moment of Fe may be arranged antiparallel to that of Co. As shown in Fig. 3(a), the magnetization of ZFC measured under a magnetic field of 100 Oe increases with the decrease of temperature around 76 K, maybe because the magnetic moment of Fe aligned antiparallel to Co reorients from the c-axis direction toward the ab plane. In addition, the magnetic moments of Fe and Co are aligned antiparallel to each other, which may be the other reason for the weakened magnetism caused by the Fe doping.

The atom-orbital-projected density of states for $Co_3Sn_2S_2$ and $Co_{2.5}Fe_{0.5}Sn_2S_2$ are shown in Figs. 11(b) and 11(d). The DOS near the Fermi level of $Co_3Sn_2S_2$ is dominated by Co-3d orbitals with the contribution from a small amount of Sn-5p and S-3p orbitals. The contribution of Fe-3d orbitals to the density of states appears near the Fermi level for $Co_{2.5}Fe_{0.5}Sn_2S_2$. Meanwhile, Fe doping also causes the change of energy band structure near the Fermi level. The hybridization between the 3d orbitals of Fe and Co with Sn-5p and S-3p orbitals opens up a channel for the itinerant ferromagnetism and may also be an important factor for the long-range $J(r)$ of $Co_{2.5}Fe_{0.5}Sn_2S_2$ [29].

IV. CONCLUSIONS

The magnetic properties, the magnetocaloric effect, and the critical behavior of the $Co_{2.5}Fe_{0.5}Sn_2S_2$ single crystal were studied, and the related mechanism was revealed by the first-principles calculation. This paper provides an important indication to understanding the itinerant ferromagnetism of magnetic Weyl semimetal $Co_3Sn_2S_2$.

In the case of $H \| c$, the saturation magnetic moment M_s at $T = 5$ K is 0.16 μ_B/Co(Fe), close to that from the theoretical calculation (0.18 μ_B/atom). The Rhodes-Wolfarth ratio proves the itinerant ferromagnetic characteristics below T_c. The remanence ratio ($M_r/M_s = 0.99$) confirms the uniaxial anisotropy. The magnetization below T_c is completely polarized into ferromagnetic order when $H > 1$ kOe. The Arrott and $n(T)$ plots especially the critical behavior analysis provide the evidence for the second-order magnetic phase

TABLE V. The magnetic moments of $Co_3Sn_2S_2$ and $Co_{2.5}Fe_{0.5}Sn_2S_2$ are obtained by calculation.

m (μ_B/atom)	Co_1	Co_2	Co_3	Co_4	Co_5	Co6/Fe
$Co_3Sn_2S_2$	0.434	0.434	0.356	0.356	0.274	0.274 (Co)
$Co_{2.5}Fe_{0.5}Sn_2S_3$	0.333	0.231	0.237	0.237	0.319	−0.265 (Fe)

transition near T_c as $H \| c$. The critical exponents ($\beta = 0.473$, $\gamma = 1.102$, and $\delta = 3.302$) show that the magnetization below T_c accords with the mean-field model, indicative of the long-range ferromagnetic interaction in $Co_{2.5}Fe_{0.5}Sn_2S_2$. The exchange interaction distance $J(r) \approx r^{-4.6469}$ is basically consistent with that for the mean-field model, i.e., $J(r) \approx r^{-4.5}$, further confirming the long-range ferromagnetic interaction of $Co_{2.5}Fe_{0.5}Sn_2S_2$. The hybridization between the $3d$ orbitals of Fe and Co with Sn-$5p$ and S-$3p$ orbitals may be an important factor for the long-range itinerant ferromagnetism.

In the case of $H \| ab$, the ZFC magnetization undergoes the spin reorientation near 76 K as $H = 100$ Oe, i.e., the out-of-plane magnetic moment of Fe turns toward in plane. Correspondingly, the local maximum of magnetic entropy change $-\Delta S_M$ appears at 77 K. The reduced temperature θ-dependent $\Delta S_M/\Delta S_M^{\max}$ curves do not overlap below T_c, revealing the magnetic transition on the *ab* plane is accompanied by the first-order phase transition.

ACKNOWLEDGMENTS

The authors thank Y. Han and Y. Liu (Anhui Province Key Laboratory of Condensed Matter Physics at Extreme Conditions, High Magnetic Field Laboratory, Chinese Academy of Sciences) for the specific heat test and resistivity measurements. This work was supported by the National Natural Science Foundation of China (Grant No. U19A2093) and the open fund for Discipline Construction, Institute of Physical Science and Information Technology, Anhui University.

[1] E. K. Liu, Y. Sun, N. Kumar, L. Muechler, A. L. Sun, L. Jiao, S. Y. Yang, D. F. Liu, A. J. Liang, Q. N. Xu, J. Kroder, V. Süß, H. Borrmann, C. Shekhar, Z. S. Wang, C. Y. Xi, W. H. Wang, W. Schnelle, S. Wirth, Y. L. Chen, S. T. B. Goennenwein, and C. Felser, Giant anomalous Hall effect in a ferromagnetic kagome-lattice semimetal, Nat. Phys. **14**, 1125 (2018).

[2] R. Weihrich, R. Pçttgen, and F. Pielnhofer, From laboratory press to spins with giant effects, Angew. Chem. Int. Ed. **57**, 15642 (2018).

[3] Q. Wang, Y. F. Xu, R. Lou, Z. H. Liu, M. Li, Y. B. Huang, D. W. Shen, H. M. Weng, S. C. Wang, and H. C. Lei, Large intrinsic anomalous Hall effect in half-metallic ferromagnet $Co_3Sn_2S_2$ with magnetic Weyl fermions, Nat. Commun. **9**, 3681 (2018).

[4] S. N. Guin, P. Vir, Y. Zhang, N. Kumar, S. J. Watzman, C. G. Fu, E. K. Liu, K. Manna, W. Schnelle, J. Gooth, C. Shekhar, Y. Sun, and C. Felser, Zero-field nernst effect in a ferromagnetic kagome-lattice weyl-semimetal $Co_3Sn_2S_2$, Adv. Mater. **31**, 1806622 (2019).

[5] Y. Okamura, S. Minami, Y. Kato, Y. Fujishiro, Y. Kaneko, J. Ikeda, J. Muramoto, R. Kaneko, K. Ueda, V. Kocsis, N. Kanazawa, Y. Taguchi, T. Koretsune, K. Fujiwara, A. Tsukazaki, R. Arita, Y. Tokura, and Y. Takahashi, Giant magneto-optical responses in magnetic Weyl semimetal $Co_3Sn_2S_2$, Nat. Commun. **11**, 4619 (2020).

[6] J. Corps, P. Vaqueiro, and A. V. Powell, $Co_3M_2S_2$ (M = Sn, In) shandites as tellurium-free thermoelectrics, J. Mater. Chem. A **1**, 6553 (2013).

[7] P. Mangelis, P. Vaqueiro, and A. V. Powell, Improved thermoelectric performance through double substitution in shandite-type mixed-metal sulfides, ACS Appl. Energy Mater. **3** (2019), pp. 2168.

[8] O. V. Yazyev, An upside-down magnet, Nat. Phys. **15**, 424 (2019).

[9] J. Tang, Y. D. Wu, W. W. Wang, L. Y. Kong, B. Y. Lv, W. S. Wei, J. D. Zang, M. L. Tian, and H. F. Du, Magnetic skyrmion bundles and their current-driven dynamics, Nat. Nanotechnol. **16**, 1086 (2021).

[10] W. S. Wei, Z. D. He, Z. Qu, and H. F. Du, Dzyaloshinsky–Moriya interaction (DMI)-induced magnetic skyrmion materials, Rare Met. **40**, 3076 (2021).

[11] W. W. Wang, D. S. Song, W. S. Wei, P. F. Nan, S. L. Zhang, B. H. Ge, M. L. Tian, J. D. Zang, and H. F. Du, Electrical manipulation of skyrmions in a chiral magnet, Nat. Commun. **13**, 1593 (2022).

[12] C. Liu, J. L. Shen, J. C. Gao, C. J. Yi, D. Liu, T. Xie, L. Yang, S. Danilkin, G. C. Deng, W. H. Wang, S. L. Li, Y. G. Shi, H. M. Weng, E. K. Liu, and H. Q. Luo, Spin excitations and spin wave gap in the ferromagnetic Weyl semimetal $Co_3Sn_2S_2$, Sci. China-Phys. Mech. Astron. **64**, 217062 (2021).

[13] Z. Guguchia, J. A. T. Verezhak, D. J. Gawryluk, S. S. Tsirkin, J. X. Yin, I. Belopolski, H. Zhou, G. Simutis, S. S. Zhang, T. A. Cochran, G. Chang, E. Pomjakushina, L. Keller, Z. Skrzeczkowska, Q. Wang, H. C. Lei, R. Khasanov, A. Amato, S. Jia, T. Neupert, H. Luetkens, and M. Z. Hasan, Tunable anomalous Hall conductivity through volume-wise magnetic competition in a topological kagome magnet, Nat. Commun. **11**, 559 (2020).

[14] E. Lachman, R. A. Murphy, N. Maksimovic, R. Kealhofer, S. Haley, R. D. McDonald, J. R. Long, and J. G. Analytis, Exchange biased anomalous Hall effect driven by frustration in a magnetic kagome lattice, Nat. Commun. **11**, 560 (2020).

[15] G. S. Thakur, P. Vir, S. N. Guin, C. Shekhar, R. Weihrich, Y. Sun, N. Kumar, and C. Felser, Intrinsic anomalous hall effect in Ni-substituted magnetic Weyl semimetal $Co_3Sn_2S_2$, Chem. Mater. **32**, 1612−1617 (2020).

[16] M. A. Kassem, Y. Tabata, T. Waki, and H. Nakamura, Structure and magnetic properties of flux grown single crystals of $Co_{3-x}Fe_xSn_2S_2$ shandites, J. Solid State Chem. **233**, 8 (2016).

[17] T. Kubodera, H. Okabe, Y. Kamihara, and M. Matoba, Ni substitution effect on magnetic and transport properties in metallic ferromagnet $Co_3Sn_2S_2$, Phys. B **378**, 1142 (2006).

[18] M. A. McGuire, Q. Zhang, H. Miao, W. Luo, M. Yoon, Y. H. Liu, T. Yilmaz, and E. Vescovo, Antiferromagnetic order and linear magnetoresistance in fe-substituted shandite $Co_3In_2S_2$, Chem. Mater. **33** (2021), pp. 9741−9749.

[19] Y. Yanagi, J. Ikeda, K. Fujiwara, K. Nomura, A. Tsukazaki, and M. Suzuki, First-principles investigation of magnetic and transport properties in hole-doped shandite compounds $Co_3In_xSn_{2-x}S_2$, Phys. Rev. B **103**, 205112 (2021).

[20] F. Pielnhofer, J. Rothballer, P. Peter, W. J. Yan, F. M. Schappacher, R. Pöttgen, and R. Weihrich, Half antiperovskites

VI: On the substitution effects in shandites $In_xSn_{2-x}Co_3S_2$, Z. Anorg. Allg. Chem. **640**, 286 (2014).

[21] M. A. Kassem, Y. Tabata, T. Waki, and H. Nakamura, Single crystal growth and characterization of kagomé-lattice shandites $Co_3Sn_{2-x}In_xS_2$, J. Cryst. Growth **426**, 208 (2015).

[22] H. B. Zhou, G. Q. Chang, G. Q. Wang, X. Gui, X. T. Xu, J. X. Yin, Z. Guguchia, S. T. S. Zhang, T. R. Chang, H. Lin, W. W. Xie, M. Z. Hasan, and S. Jia, Enhanced anomalous Hall effect in the magnetic topological semimetal $Co_3Sn_{2-x}In_xS_2$, Phys. Rev. B **101**, 125121 (2020).

[23] M. A. Kassem, Y. Tabata, T. Waki, and H. Nakamura, Quasi-two-dimensional magnetism in co-based shandites, J. Phys. Soc. Jpn. **85**, 064706 (2016).

[24] R. Weihrich, W. J. Yan, J. Rothballer, P. Peter, S. M. Rommel, S. Haumann, F. Winter, C. Schwickertc, and R. Pöttgen, Tuneable anisotropy and magnetism in $Sn_2Co_3S_{2-x}Se_x$–probed by ^{119} Sn Mößbauer spectroscopy and DFT studies, Dalton Trans. **44**, 15855 (2015).

[25] Y. Sakai, Y. Kamihara, and M. Matoba, Magnetic properties of shandite-type $Co_3Sn_2S_{2-x}Se_x$, Phys. Status Solidi C **10**, 1130 (2013).

[26] A. Ali, Shama and Y. Singh, Rotating magnetocaloric effect in the ferromagnetic Weyl semi-metal $Co_3Sn_2S_2$, J. Appl. Phys. **126**, 155107 (2019).

[27] W. N. Yan, X. Zhang, Q. Shi, X. Y. Yu, Z. Q. Zhang, Q. Wang, S. Li, and H. C. Lei, Critical behavior of half-metallic ferromagnet $Co_3Sn_2S_2$, Solid State Commun. **281**, 57 (2018).

[28] Q. Shi, X. Zhang, E. Yang, J. Yan, X. Yu, C. Sun, S. Li, and Z. Chen, Study of magnetocaloric effect in half-metallic ferromagnet $Co_3Sn_2S_2$, Res. Phys. **11**, 1004 (2018).

[29] S. Lin, H. Y. Lv, J. C. Lin, Y. N. Huang, L. Zhang, W. H. Song, P. Tong, W. J. Lu, and Y. P. Sun, Critical behavior in the itinerant ferromagnet $AsNCr_3$ with tetragonal-antiperovskite structure, Phys. Rev. B **98**, 014412 (2018).

[30] V. K. Pecharsky, K. A. Gschneidner, Jr. A. O. Pecharsky, and A. M. Tishin, Thermodynamics of the magnetocaloric effect, Phys. Rev. B **64**, 144406 (2001).

[31] P. Bag A.Dey, P. Kalita, and V. Chandrasekhar, Heterometallic $Cu^{II} - Ln^{III}$ complexes: Single molecule magnets and magnetic refrigerants, Coord. Chem. Rev. **432**, 213707 (2021).

[32] A. M. Aliev, L. N. Khanov, A. G. Gamzatov, A. B. Batdalov, D. R. Kurbanova, K. I. Yanushkevich, and G. A. Govor, Giant magnetocaloric effect in $MnAs_{1-x}P_x$ in a cyclic magnetic field: Lattice and magnetic contributions and degradation of the effect, Appl. Phys. Lett. **118**, 072404 (2021).

[33] N. A. Zarkevich and V. I. Zverev, Viable materials with a giant magnetocaloric effect, Cryst. **10**, 815 (2020).

[34] I. Hussain, M. S. Anwar, S. R. Lee, and B. H. Koo, Effect of Zn on the magnetic and magnetocaloric properties of $(0.95)La_{0.7}Ca_{0.3}MnO_3/(0.05)Mn_{1-x}Zn_xFe_2O_4$ composites, J. Supercond. Nov. Magn. **28**, 3323 (2015).

[35] T. Isono, S. Sugiura, T. Terashima, K. Miyagawa, K. Kanoda, and S. Uji, Spin-lattice decoupling in a triangular-lattice quantum spin liquid, Nat. Commun. **9**, 1509 (2018).

[36] J. Y. Hu, X. C. Kan, Z. Chen, G. H. Zheng, and Y. Q. Ma, The magnetic, thermal transport properties, magnetocaloric effect and critical behavior of $Co_3Sn_2S_2$ single crystal, J. Am. Ceram. Soc. **105**, 4827 (2022).

[37] S. Rathod, A. Lakhani Megha, and D. Kumar, Crystal growth and characterization of novel magnetic half-metallic semimetal $Co_3Sn_2S_2$, *3rd International Conference on Condensed Matter and Applied Physics (ICC-2019)*, AIP Conf. Proc. 2220 (AIP, Melville, NY, 2020), p. 060007.

[38] J. L. Shen, Q. Q. Zeng, S. Zhang, H. Y. Sun, Q. S. Yao, X. K. Xi, W. H. Wang, G. H. Wu, B. G. Shen, Q. H. Liu, and E. K. Liu, 33% giant anomalous hall current driven by both intrinsic and extrinsic contributions in magnetic weyl semimetal $Co_3Sn_2S_2$, Adv. Funct. Mater. **30**, 2000830 (2020).

[39] M. A. Kassem, Y. Tabata, T. Waki, and H. Nakamura, Unconventional critical behaviors at the magnetic phase transition of $Co_3Sn_2S_2$ kagomé ferromagnet, J. Phys.: Condens. Matter **33**, 015801 (2020).

[40] X. Lin, V. Taufour, S. L. Bud'ko, and P. C. Canfield, Suppression of ferromagnetism in the $LaV_xCr_{1-x}Ge_3$ system, Phys. Rev. B **88**, 094405 (2013).

[41] P. Rhodes and E. P.Wohlfarth, The effective Curie-Weiss constant of ferromagnetic metals and alloys, Proc. R. Soc. London Ser. A **273**, 247 (1963).

[42] A. Ezaami, I. Chaaba, W. Cheikhrouhou-Koubaa, A. Cheikhrouhou, and E. K. Hlil, Enhancement of magnetocaloric properties around room temperature in $(1\text{-}x)La_{0.7}Ca_{0.25}Sr_{0.05}MnO_3/xLa_{0.7}Ca_{0.2}Sr_{0.1}MnO_3$ system ($0 \leqslant x \leqslant 1$), J. Alloys Compd. **735**, 2331 (2018).

[43] B. S. Wang, J. C. Lin, P. Tong, L. Zhang, W. J. Lu, X. B. Zhu, Z. R. Yang, W. H. Song, J. M. Dai, and Y. P. Sun, Structural, magnetic, electrical transport properties, and reversible room-temperature magnetocaloric effect in antipervoskite compound $AlCMn_3$. J. Appl. Phys. **108**, 093925 (2010).

[44] D. D. Belyea, M. Lucas, E. Michel, J. Horwath, and C. W. Miller, Tunable magnetocaloric effect in transition metal alloys, Sci. Rep. **5**, 15755 (2015).

[45] S. Lin, B. S. Wang, J. C. Lin, L. Zhang, X. B. Hu, Y. N. Huang, W. J. Lu, B. C. Zhao, P. Tong, W. H. Song, and Y. P. Sun, Composition dependent-magnetocaloric effect and low room-temperature coefficient of resistivity study of iron-based antiperovskite compounds $Sn_{1-x}Ga_xCFe_3$ ($0 \leqslant x \leqslant 1.0$), Appl. Phys. Lett. **99**, 172503 (2011).

[46] W. Tang, W. J. Lu, X. Luo, B. S. Wang, X. B. Zhu, W. H. Song, Z. R. Yang, and Y. P. Sun, Particle size effects on $La_{0.7}Ca_{0.3}MnO_3$: Size-induced changes of magnetic phase transition order and magnetocaloric study, J. Magn. Magn. Mater. **322**, 2360 (2010).

[47] V. K. Pecharsky and K. A. Gschneidner, Jr., Magnetocaloric effect and magnetic refrigeration, J. Magn. Magn. Mater. **200**, 44 (1999).

[48] S. Ghosh and S. Ghosh, Giant magnetocaloric effect driven by first-order magnetostructural transition in cosubstituted Ni-Mn-Sb Heusler compounds: Predictions from *ab initio* and Monte Carlo calculations, Phys. Rev. B **103**, 054101 (2021).

[49] J. C. Debnath, R. Zeng, J. H. Kim, D. P. Chen, and S. X. Dou, Anisotropic and excellent magnetocaloric properties of $La_{0.7}Ca_{0.3}MnO_3$ single crystal with anomalous magnetization, Mater. Sci. Eng. B **177**, 48 (2012).

[50] J. Y. Law, V. Franco, L. M. Moreno-Ramírez, A. Conde, D. Y. Karpenkov, I. Radulov, K. P. Skokov, and O. Gutfleisch, A quantitative criterion for determining the order of magnetic phase transitions using the magnetocaloric effect, Nat. Commun. **9**, 2680 (2018).

[51] H. Oesterreicher and F. T. Parker, Magnetic cooling near Curie temperatures above 300 K, J. Appl. Phys. **55**, 4334 (1984).

[52] H. Han, D. Menze, W. Liu, L. S. Ling, H. F. Du, L. Pi, C. J. Zhang, L. Zhang, and Y. H. Zhang, Scaling of the magnetic entropy change in skyrmion material $Fe_{0.5}Co_{0.5}Si$, Mater. Res. Bull. **94**, 500 (2017).

[53] M. Seeger, S. N. Kaul, and H. Kronmuller, Asymptotic critical behavior of Ni, Phys. Rev. B **51**, 12585 (1995).

[54] J. S. Kouvel and M. E. Fisher, Detailed magnetic behavior of nickel near its curie point, Phys. Rev. **136**, A1626 (1964).

[55] H. E. Stanley, *Introduction to Phase Transitions and Critical Phenomena* (Oxford University Press, London, 1971).

[56] L. P. Kadanoff, Scaling laws for ising models near T_c, Physica **2**, 263 (1966).

[57] A. Arrott and J. E. Noakes, Approximate Equation of State for Nickel Near its Critical Temperature, Phys. Rev. Lett. **19**, 786 (1967).

[58] L. Zhang, B. Wang, Y. Sun, P. Tong, J. Fan, C. Zhang, L. Pi, and Y. Zhang, Critical behavior in the antiperovskite ferromagnet $AlCMn_3$, Phys. Rev. B **85**, 104419 (2012).

[59] W. Wang, X. C. Kan, X. S. Liu, Z. T. Zhang, K. M. U. Rehman, C. C. Liu, and M. Shezad, Ferromagnetic frustration in ternary nitride $ZnFe_3N$, Phys. Chem. Chem. Phys. **22**, 27770 (2020).

[60] K. Ghosh, C. J. Lobb, R. L. Greene, S. G. Karabashev, D. A. Shulyatev, A. A. Arsenov, and Y. Mukovskii, Critical Phenomena in the Double-Exchange Ferromagnet $La_{0.7}Sr_{0.3}MnO_3$, Phys. Rev. Lett. **81**, 4740 (1998).

[61] M. E. Fisher, S. K. Ma, and B. G. Nickel, Critical Exponents for Long-Range Interactions, Phys. Rev. Lett. **29**, 917 (1972).

[62] A. K. Pramanik and A. Banerjee, Critical behavior at paramagnetic to ferromagnetic phase transition in $Pr_{0.5}Sr_{0.5}MnO_3$: A bulk magnetization study, Phys. Rev. B **79**, 214426 (2009).

[63] S. Mondal, N. Khan, S. M. Mishra, B. Satpati, and P. Mandal, Critical behavior in the van der Waals itinerant ferromagnet Fe_4GeTe_2, Phys. Rev. B **104**, 094405 (2021).

[64] B. Chen, J. H. Yang, H. D. Wang, M. Imai, H. Ohta, C. Michioka, K. Yoshimura, and M. H. Fang, Magnetic properties of layered itinerant electron ferromagnet Fe_3GeTe_2, J. Phys. Soc. Jpn. **82**, 124711 (2013).

[65] H. Ohta, C. Michioka, A. Matsuo, K. Kindo, and K. Yoshimura, Magnetic study of SmCoAsO showing a ferromagnetic-antiferromagnetic transition, Phys. Rev. B **82**, 054421 (2010).

[66] M. Imai, C. Michioka, H. Ueda, and K. Yoshimura, Static and dynamical magnetic properties of the itinerant ferromagnet $LaCo_2P_2$, Phys. Rev. B **91**, 184414 (2015).

[67] H. Ohta and K. Yoshimura, Anomalous magnetization in the layered itinerant ferromagnet LaCoAsO, Phys. Rev. B **79**, 184407 (2009).

[68] P. Mangelis, P. Vaqueiro, J. C. Jumas, I. Silva, R. I. Smith, and Anthony V. Powell, The effect of electron and hole doping on the thermoelectric properties of shandite-type $Co_3Sn_2S_2$, J. Solid State Chem. **251**, 204 (2017).

[69] H. Rosner, R. Weht, M. D. Johannes, W. E. Pickett, and E. Tosatti, Superconductivity Near Ferromagnetism in $MgCNi_3$, Phys. Rev. Lett. **88**, 027001 (2001).